Developmental Cell
Short Article

# Mechanistic Basis of Otolith Formation during Teleost Inner Ear Development

David Wu,[1] Jonathan B. Freund,[2] Scott E. Fraser,[1] and Julien Vermot[3,*]
[1]Biological Imaging Center, Beckman Institute, Option in Bioengineering, Caltech, Pasadena, CA 91125, USA
[2]University of Illinois at Urbana-Champaign, Urbana, IL 61801, USA
[3]Institut de Génétique et de Biologie Moléculaire et Cellulaire (IGBMC), Institut National de Santé et de Recherche Médicale (INSERM) U964/Centre National de Recherche Scientifique (CNRS) UMR 1704/Université de Strasbourg, 67404 Illkirch, France
*Correspondence: julien@igbmc.fr
DOI 10.1016/j.devcel.2010.12.006

## SUMMARY

**Otoliths, which are connected to stereociliary bundles in the inner ear, serve as inertial sensors for balance. In teleostei, otolith development is critically dependent on flow forces generated by beating cilia; however, the mechanism by which flow controls otolith formation remains unclear. Here, we have developed a noninvasive flow probe using optical tweezers and a viscous flow model in order to demonstrate how the observed hydrodynamics influence otolith assembly. We show that rotational flow stirs and suppresses precursor agglomeration in the core of the cilia-driven vortex. The velocity field correlates with the shape of the otolith and we provide evidence that hydrodynamics is actively involved in controlling otolith morphogenesis. An implication of this hydrodynamic effect is that otolith self-assembly is mediated by the balance between Brownian motion and cilia-driven flow. More generally, this flow feature highlights an alternative biological strategy for controlling particle localization in solution.**

## INTRODUCTION

Biominerals are diverse materials that give shape, rigidity, and functionality of numerous specialized organs (Bouligand, 2004). Their material properties and design have played an important role in the evolutionary success of vertebrates (Wilt, 2005). Yet the biological mechanisms that control biomineralization are poorly understood. The most obvious type of biominerals in vertebrates is bone but many other structures rely on mineral aggregation such as teeth, carapaces, and otoliths. Multiple types of biomineralization processes have been described to explain the genesis of the multiplicity of shapes, sizes, and compositions of organic and mineral components that come out of the biomineralization process. In particular, the otoliths in teleost are ovoid biominerals which form the ear stone or otoconia located in the vestibular labyrinth of the inner ear. They are millimeter-sized particles, composed of calcium carbonate and an organic matrix made of glycoproteins, proteoglycans, and collagens (Hughes et al., 2006), and they provide an inertial mass that facilitates deflection of ciliary bundles in response to vibration, gravity and linear acceleration essential for hearing and balance.

In zebrafish, early growth of otoliths is tightly controlled in time, with a period of fast growth between 19 and 24 hr after fertilization (hpf). Saturating growth occurs for the rest of the fish's adult life (Riley et al., 1997). The otic cavity contains precursor 1-3 micron particles, or spherules, secreted from the apical portions of the epithelial cells of the inner ear (Riley et al., 1997). Time-lapse analysis and electron microscopy show that otolith growth starts as a nucleus of spherules aggregating at the top of a tether cilium (Clendenon et al., 2009; Pisam et al., 2002). At 30 hpf, a mineralized ovoid otolith is visible (Pisam et al., 2002; Sollner et al., 2003) and concentric arrays of spherule deposition are seen at the periphery of the nascent otolith (Pisam et al., 2002).

The early process of otolith assembly (19-24 hpf) is particularly interesting because it requires the presence of biological flow generated by beating cilia (Colantonio et al., 2009; Riley et al., 1997). The otolith-forming region has a specific topology: a cluster of motile cilia located next to the tether, stationary cilia at each pole (anterior and posterior) of the ovoid-inner ear (Colantonio et al., 2009). The inner ear also contains shorter cilia lining the entire vesicle that are immotile (Colantonio et al., 2009). Previous experiments demonstrated that motile cilia are essential for normal otolith number, size, and position (Colantonio et al., 2009). However, the roles of flow for the mechanism of otolith formation during the period of fast growth is not yet well understood. It was first proposed that the motile cilia act as a dispersant to mix fluid and spherules throughout the inner ear (Riley et al., 1997). More recently, it was suggested that motile cilia act locally as dynamic attractors of spherules and that flow at the poles increases the likelihood of spherules to meet the tether cilia (Colantonio et al., 2009). Nevertheless, the hydrodynamic basis of spherule transport toward the otolith and the role of cilia mixing remains unclear in this model. Furthermore, while it seems that the position, size, and number of otoliths in any given inner ear could be controlled by beating cilia (Colantonio et al., 2009), it is still unclear if flow can account for otolith shape.

In this study, we developed a flow probe based on optical tweezers to assess the fluid dynamics at work in the inner ear. This approach allowed us to define two hydrodynamic features essential for otolith formation. First, a global, vortical flow generated around the tether cilia favors spherule transport toward the

growing otolith. Second, a local mixing flow located at the base of the forming otolith paradoxically reduces agglomeration. Diffusion dominates outside this stirred region, allowing for agglomeration of the transported spherules. Finally, we use a simple physical model to clarify the role of cilia in the process of spherule transport. Altogether, these results suggest that the dual action of stirring and vortical flow cause the otolith to take on its typical shape and establish the hydrodynamic basis of asymmetric transport through cilia-mediated flow in the inner ear of zebrafish.

## RESULTS

### Mapping Inner Ear Flow Reveals Motile Cilia Transport of Spherules toward Tether Cilia

The relative strength of deterministic flows relative to the stochastic motion of the spherules is parameterized by the Peclet number, $Pe = v_{max}l/D$, ($v_{max}$ is the maximum velocity in the system, $l$- the diameter of the observed particle, and $D$- the diffusion constant). A system with $Pe << 1$ is primarily diffusive, whereas a system with $Pe >> 1$ is advective, dominated by flow. Near the motile cilia, the maximum inner ear $Pe$ can reach upward of 60–100, as determined by cilium speed, assuming a particle with the lateral dimension of a cilium, and its medium of travel being water. We tested two implications of such a $Pe$ for otolith biogenesis: namely, whether (1) the rapid reduction in flow propagation, due to the viscous nature of inner ear fluid, results in a transition to dominantly Brownian motion near the tether cilia, and therefore correlates with otolith nucleation, and whether (2) the high velocity of motile cilia in an enclosed structure results in spherule localization near the tether cilia in vivo.

To investigate the nature of the cilia-induced flow propagation, we developed a noninvasive strategy to visualize the paths followed by spherules near the motile cilia. We used in vivo optical trapping within the inner ear in order to accumulate hundreds of spherules and release them into the flow field, much as smoke can be used to visualize the flow field around a car in a wind tunnel (Figures 1A–1E). We trapped spherules at 1064 nm, a nonphototoxic wavelength (Svoboda and Block, 1994), so that embryonic (n = 6) and otolith development was not affected when compared with nonmanipulated siblings (n = 11). This approach allowed us to generate and map the time-averaged (stationary) flow field (Figures 1F–1J; see Movies S1–S3 available online) and show that spherules are propelled through fluid along helical paths inside the cavity. When trapped further from the cilia, we see spherules advected toward the cilia and becoming entrained in the vortical flow, effectively localizing spherules near the nascent otolith (Figures 1G and 1J; Movies S2 and S3). The time for one revolution of released particles was T = 4.6 ± .9 s, although the cilia beating frequency was much faster, at 44 ± 4 Hz. A clear separation between a disordered and an ordered regimen was seen (Figure 1F; Movies S2 and S3). The deterministic portion of the induced flow encompasses the near field of the cilia next to the otolith (3.1 ± 0.5 microns) and drops off quickly into purely diffusive behavior (to 10% of the maximum velocity, as measured by particle image velocimetry), as shown by the transition from correlated to uncorrelated vectors in Figures 1F and 1G. Similar flow patterns were observed for anterior and posterior otoliths. Altogether, these data suggest that the flow can affect the transport of spherules toward and about the growing otolith (Figure 1K).

### The Otolith Emerges at the Juxtaposition between the Well-Stirred Near Field and the Diffusion-Dominated Far Field

In order to mark the transition between diffusion-dominated versus advection-dominated flow, we investigated spherule behavior around the otolith independent of the global streamlines, by examining shorter time periods of motion. By using the blinking optical trap technique (BOTs) (Lin et al., 2000), we measured spherules' mean-squared displacement (MSD) behavior at a single point over 30 ms (Figures 2A–2I; Movie S4) for a range of positions in the inner ear. This technique is ideally suited for performing in vivo MSD measurements, as there is no requirement for knowing the precise optical and hydrodynamic properties of the system a priori. By fitting the MSD to a Langevin model of fluid motion

$$\left\langle x(t)^2 \right\rangle \approx 2Dt + \frac{a_c^2}{\omega^2}(1 - \cos\omega t),$$

we were able to extract the relevant physical parameters (Figures 2G and 2H) and generate short-time flow maps (Figure 2I): $D$ is the diffusion coefficient, $a_c$ is the local amplitude of the oscillating velocity, and $\omega$ is the frequency of the oscillation (see Supplemental Experimental Procedures and Figure S1). Fit parameter $a_c$ quantifies the degree of influence the motile cilia exert on the interrogation point of the BOTs (Figures 2D–2F and 2I) and serves as a way to map the field strength of the cilia beat in the absence of global flows (Figure 2I). The fitted parameters were strikingly similar to measured and expected parameters in vivo (frequency, $\omega$, 43, ±8.6 Hz, and diffusion coefficient, $D$, 0.1 ± 0.1 $\mu m^2$/sec), thereby allowing us to use the $a_c$ fitted parameter with confidence. Note that motile cilia circumscribe a ~3–5 micron trajectory at their tip; at 43 Hz, this corresponds to speeds up to 33 $\mu$m/sec. We found that flows induced by the motile cilia dropped to within 10% of their initial value in less than 4 $\mu$m (Figure 2I); this corresponds to the thickness of the advection dominant zone in the zebrafish inner ear. The otolith, always located within a few microns of the motile cilia, thus emerges at the juxtaposition between the well-stirred near field and the diffusion dominated far field, which is determined by the physical parameters of the cilia.

### Fluid Mixing Is Necessary to Prevent Agglomeration and Controls Otolith Shape

To gain insight into the physiological role of cilia-induced fluid mixing in controlling otolith shape, we addressed the aftereffects of motile cilia ablation during the period of rapid otolith growth (18–24 hpf) (Riley et al., 1997). Since the otolith acts as a self-aggregation point, we used focal laser ablation to inactivate motile cilia beating after nucleation occurred (Figures 3A–3D; Movie S5) and addressed the effect of flow cessation on otolith shape. The primary process of diffusion-limited aggregation ($Pe << 1$) is less dependent on cilia-induced flow since we found that total growth was not significantly affected by cilia ablation (Figures 3E–3K). In order to analyze the shape of the otolith, we segmented the otolith shape before and after laser

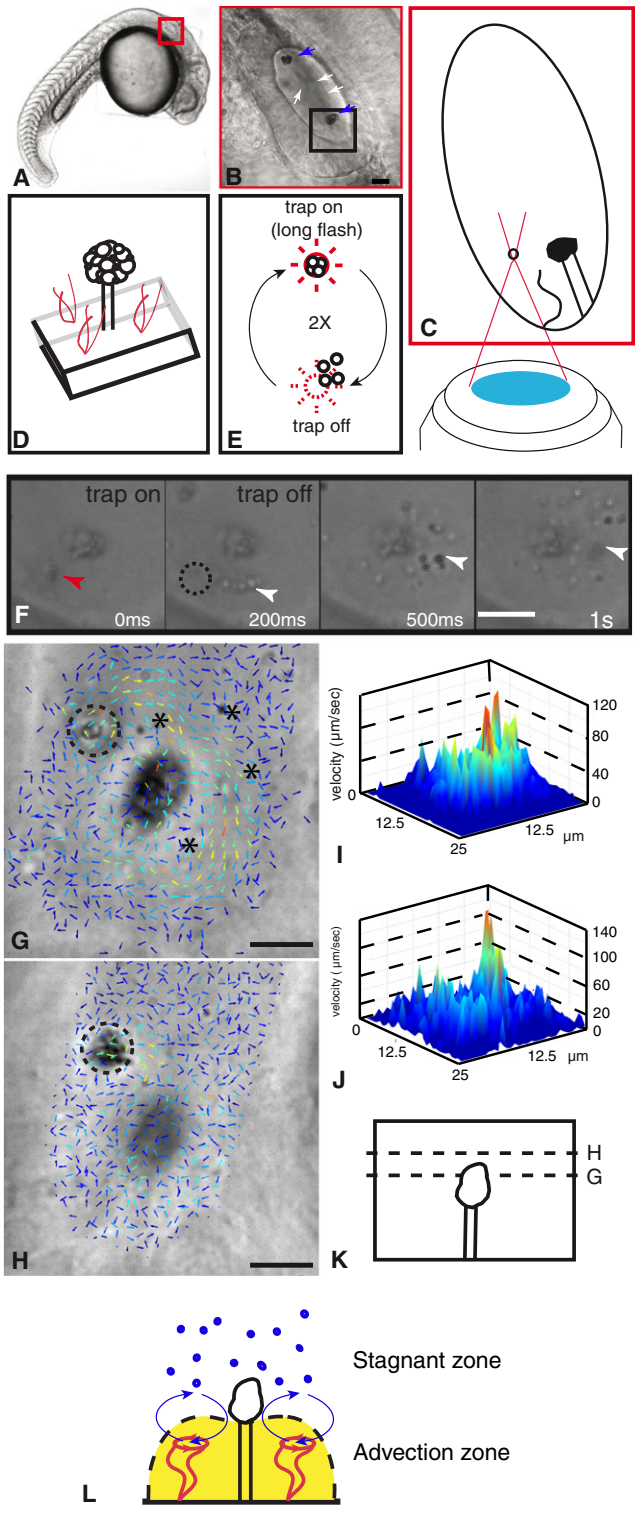


**Figure 1. Mapping the Global Flow Field of the Inner Ear**

(A) Side view of a zebrafish embryo at the stage (18–24 hpf) of optical tweezing. The red box outlines the inner ear.

(B) Magnified version of the inner ear corresponding to the red box in (A). White arrows point to spherules, which are numerous at this stage, and blue arrows point to the otoliths.

(C) Schematic view of the optical tweezing approach, depicting the use of focused light to position spherules in the inner ear.

(D) Cilia implantation next to the otolith. Drawing depicting motile cilia (in red) position with respect to tether cilia (in back) and otolith (depicted as an aggregates of spherules).

(E) Parcels of spherules are aggregated using the optical trap for up to 30 s and positioned at a desired location in the inner ear. The trap is then turned off and the particles are "released" following the flow field generated by beating cilia (F). See also Movie S1. In order to compute the flow maps as depicted in (G) and (H), this process was repeated at least twice near each otolith.

(F) A montage sequence of released particles near a motile cilium in a side viewed embryo. White arrows show released particles that were trapped initially (red arrowhead, upper left box) and followed through a 1 s (upper right box, lower left box, lower right box, respectively) sequence after trap is turned off (dotted lines).

(G and H) Particle image velocimetry (PIV) of the flow field near an otolith inside a typical inner ear viewed dorsally, calculated from released particles. See Movies S2 and S3 for comparison. In (G), the trapped particles (dotted lines) were placed in the plane of the otolith; this is indicated in the schematic (K) which depicts an orthogonal cut through the inner ear. Particles are advected into the flow field (yellow arrows), indicating that the cilia have the ability to localize particles near the nascent otolith. Asterisks point to motile cilia underlined by the rotational flow observed in Movie S1. In (H), the trapped particles (dotted lines) are displaced 5 microns from the plane otolith, as depicted in schematic (K). Particles are still able to be advected into the otolith region (yellow arrows). This is better shown in the supplemental movies. Note that in the center of the high-advection region of (G) is an area of low flow (blue arrows), indicating that stagnation occurs near the otolith.

(I and J) The magnitude of the velocities of the images shown in (G) and (H) are displayed in surface relief along the z axis. The color of the arrows in (G) and (H) correspond directly to peaks in (I) and (J), respectively. The xy axis in (I) and (J) represents the dimension of the G and H images, respectively. There is a much broader area of large velocity magnitude in (G) compared with (H), indicating that the flow field far from the otolith is strongly diffusive. The gradient of velocities changes from tens of microns per second to background values within 4 microns or less.

(K) Relative position of the focal planes where the measurements were performed in (G) and (H) (5 microns distance). The red lines indicate the position of the motile cilia. (L) Schematic representation of the flow field near the motile cilia (blue arrows), spherules (blue circles), and the tether cilia attached to the growing otolith. Near field flow is advective, as denoted by the yellow shading; the far field is dominated by diffusion. Scale bars: (B) 10 microns, (F) 5 microns, (G and H) 5 microns.

ablation by measuring the mean of the sum of squared residuals (SSR) relative to a circle (Figures 3E–EJ and 3L–3M; Figures S2A–S2D and Supplemental Experimental Procedures). For this analysis, a SSR closer to 0 implies that the shape is more spherical. The mean SSR in ablated embryos was 0.31 (n = 24), and the wild-type 0.53 (n = 33). The significance of the difference was validated by a bootstrap analysis (p-value < 0.03) (see Supplemental Experimental Procedures). The difference is still visible 17 hr after ablation (Figures 3N and 3O) and is independent of the side where the ablation was performed (both anterior or posterior otoliths were ablated and the contralateral side was used as control, n = 5). Thus, a secondary effect of cilia-induced flow is the formation of an aspherical otolith, often mushroom-top shaped. These observations correspond to a subclass of otolith phenotypes observed after genetic ablation of *gas8*, an essential gene for cilia beating and inner ear development (Colantonio et al., 2009) and suggest that cilia motility is required at several steps of otolith assembly. This result implies that pure Brownian motion prefers to form a more spherical otolith, whereas directed flow (*Pe* ~ 60–100) near the tether cilia locally

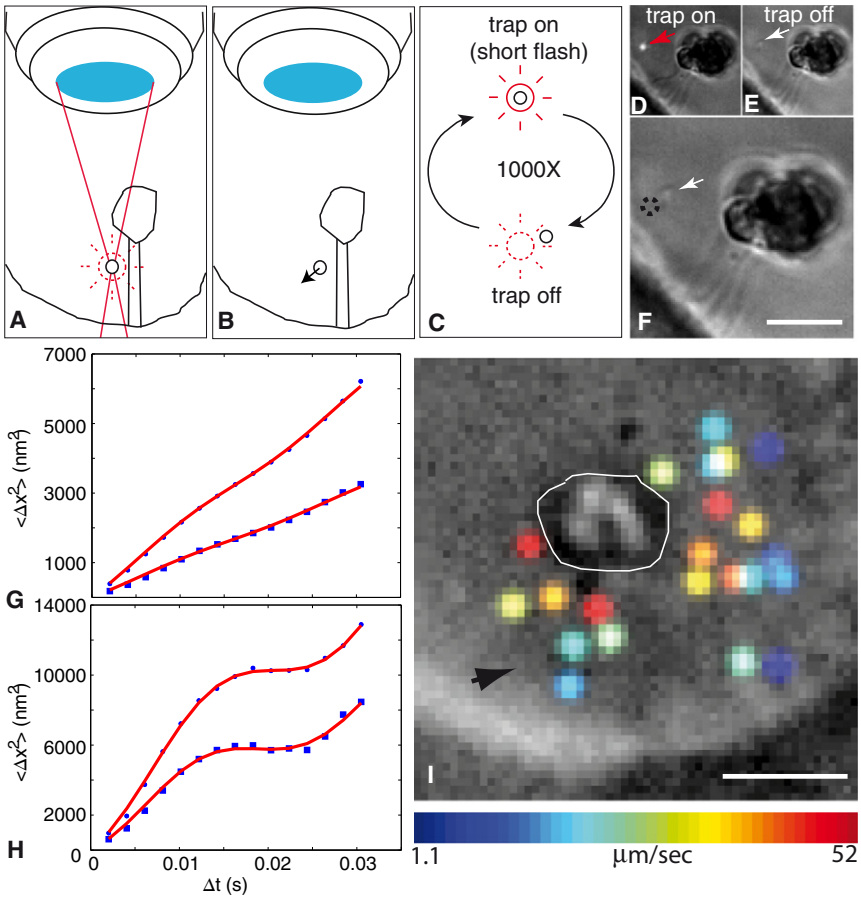


**Figure 2. Mapping Local Hydrodynamics Using Blinking Optical Traps**

(A–F) Schematic view of the optical tweezing depicting the sequence of trap and release used to measure Brownian dynamics at single point inside the inner ear. In vivo, spherules are trapped (A) and released (B) roughly 1000 times (C) at a frequency of 10 Hz, and imaged at 492 Hz, in order to resolve accurate sub-second dynamics of flow, as opposed to global flows in Figure 1 in side viewed embryos. (D) The white circle indicates the location of trapped particles (red arrow) and the white arrow in (E) points to the spherules position .002 s after release and reveals its displacement after the trap is turned off (dotted lines, F). See Movie S4 for demonstration of blinking optical traps.

(G and H) Mean-squared spherule displacement plotted as a function of time illustrating a typical diffusive spherule motion (G) and driven motion (H) in both x (circles) and y (squares). The particular curves chosen demonstrate the strong effect of boundary conditions on the Brownian dynamics. The error (standard deviation) on the MSD curves are approximately equal to the value of the MSD at each point. 30 ms of MSD was calculated at each BOTs point to avoid global flow effects (see Supplemental Experimental Procedures), as described in Figure 1.

(I) Flow map reconstituted using the BOTs model shows a velocity (parameter $a_c$) field that decays with increasing distance from the cilium (the black arrow points at the motile cilium which is better seen in Movie S4). Here, the tether cilium is not visible in this still image because it is out of focus. Note that the otolith (the central bright object) itself moves, and is therefore responsible for increased flow near itself. The velocity decreases to 10% of maximum 4 microns from the cilium. Scale bars: (F and I) 5 microns.

diminishes the spherules aggregation, resulting in the classic mushroom-top shape of zebrafish otoliths (Blasiole et al., 2006; Pisam et al., 2002; Schibler and Malicki, 2007; Sollner et al., 2003). Thus, in addition to inducing global transport of spherules to the poles of the inner ear, cilia motion induces a high-speed flow field around the tether cilia beneath the nascent otolith; stagnation areas are immediately superior, at the sides and top of the nascent otolith, because of the quick decay of cilia influence (Figure 2I). This biases spherule deposition away from the bottom of the otolith, resulting in an aspherical shape (SSR > 0) (Figure 3P).

## Stokes Flow Explains Preferential Spherule Location

An important experimental result is that spherules become entrained by the motile cilia according to their averaged trajectories in the inner ear (Figure 1F). To investigate in more detail whether flow can bias spherule localization, we used a physical model that captures the essential features of the system by simulating cilium-induced flow inside a spherical cavity. Our model for the cilium consists of a small sphere which traverses an elliptical track (Figure 4A; Vilfan and Julicher, 2006). Since the Reynolds number is much less than unity and the cilia are much smaller than the overall scale of the cavity, flow inside the inner ear can be approximated by the Stokes equation with a singular force $-\nabla p + \mu\nabla^2\mathbf{v} = -\mathbf{F}\delta(\mathbf{x}-\mathbf{x}_i)$ with constraint $\nabla\cdot\mathbf{v}=0$ ($p$ is the pressure, $\mu$ the viscosity, $\mathbf{v}(\mathbf{x})$ the velocity field, and $\mathbf{F}$ the cilium's effective point force located at $\mathbf{x}_i$ imparted by the cilium). The equation admits analytical solutions inside a sphere (Maul and Kim, 1994), which we chose to model the inner ear cavity (Figure 4B). The hydrodynamic velocity field is $\mathbf{v}(\mathbf{x}) = \mathbf{G}(\mathbf{x},\mathbf{x}_i)\mathbf{F}_i$. Here, the Green's function, $\mathbf{G}$, consists of the Oseen tensor which describes the flow generated by a singular force in a boundless fluid in addition to a complex set of terms that enforce no-slip, no penetration boundary conditions on the inside surface of the spherical inner ear (Maul and Kim, 1994) (Supplemental Information). The flow field is calculated as a time average of the cilium motion, and diffusive transport of the spherules is included using Brownian dynamics. We adjust *Pe* most easily through changing the frequency of the cilium. For the simulation, we randomly seed 1 μm particles on the cavity surface as a starting condition, which is in accordance with the origin of spherules in vivo (Pisam et al., 2002), and set parameters based on the known hydrodynamic characteristics of the inner ear (see Supplemental Information). We ran all the simulations until the system reached a statistically stationary condition, typically hundreds of seconds in real time. The model predicts that flux

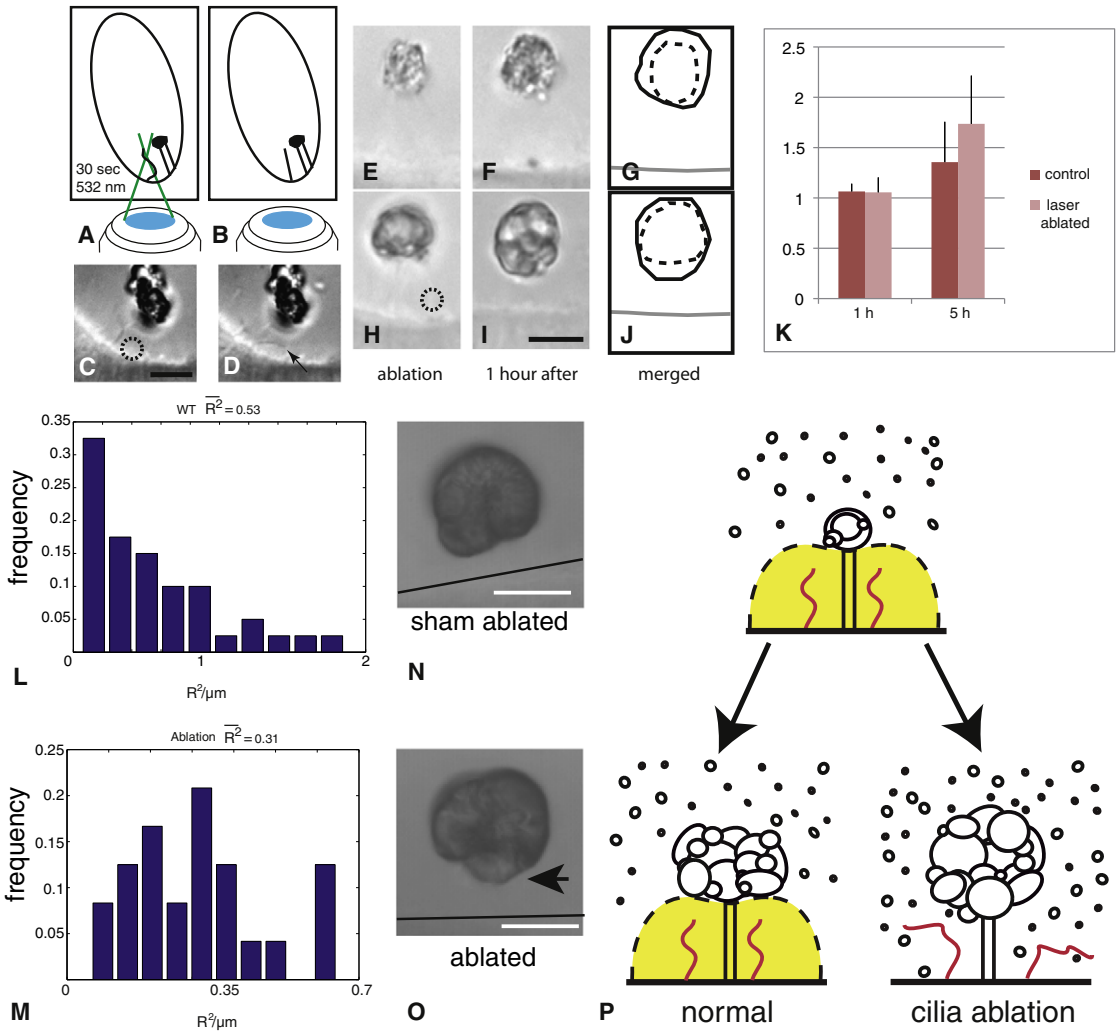


**Figure 3. Laser Ablation of Motile Cilia**

(A–D) Schematic of the experiment. A 532 nm laser was aimed squarely at the motile cilium (A and C) until the cilia paused their movement (B and D, black arrow, see Movie S5). The dotted line indicates the ablation spot (C). See Movie S5, for example.

(E and F) Control otolith before and after sham ablation.

(G–J) Otolith before (H) and after 1 hr after local cilium ablation (I). The otolith clearly grows as seen in the schematic representing the overlay of the otoliths before (dashed line) and after (solid line) 1 hr after sham ablation (G) and true ablation (J).

(K) Segmentation of the otoliths (see Supplemental Experimental Procedures) shows that ablation does not affect gross accumulation, as measured by relative area, of spherules on the growing otolith 5 hr after ablation. Errors are by standard error of the mean.

(L and M) Distribution of the otolith shape (measured in units of SSR/micron) in controls (L) and cilia ablated embryos (M) less than 5 hr after ablation shows a clear difference, confirming the necessity of cilia beat for maintaining aspherical otolith shape ($p < 0.03$) (see Supplemental Experimental Procedures).

(N and O) Shape difference 17 hr after ablation. The black line underlines the surface of the inner ear which is aligned with the otolith's flat base in control (N, black line), but not in the ablated, contralateral otolith (black arrow) (O).

(P) Schematic of the proposed mechanism for formation of aspherical otolith shape. The high-speed flow at the base of the otolith due to the motile cilia (in red) prevents agglomeration (yellow area) while diffusion in stagnant areas (white area) permits agglomeration of particles, resulting in aspherical otolith formation (normal). After cilia ablation, the otolith growths uniformly, forming a grossly circular spherical shape. Scale bars: (I, N, and O) 10 microns.

toward the region of the motile cilia is a nonlinear function of the Peclet number (Figure 4C), suggesting that motile cilia pull spherules toward the tether cilia, as shown in Movie S6. Moreover, the presence of a dipole-type of flow field increases particle circulation near the motile cilia (Figure 4D), which accounts for the entrainment observed in Figure 1F. A particle moving along a streamline at some velocity $v$ in each time interval $dt$ has probability $k \times dt$ of randomly walking off the streamline; $k$ is related to diffusion - $k \sim D/A$, where $A$ is some diffusion area. Therefore, the average distance a particle will travel on a streamline before wandering away is $v/k$. For a circulating streamline of radius $r$, the average number of times a particle will circulate cilia is thus $< N_{circ} > = v/(2\pi rk)$. Since the streamlines have smaller radii and faster velocity near the motile cilium (Figures 4D–4F), particles near the motile cilium will, on average, circulate around the cilium more times than particles traveling on streamlines far

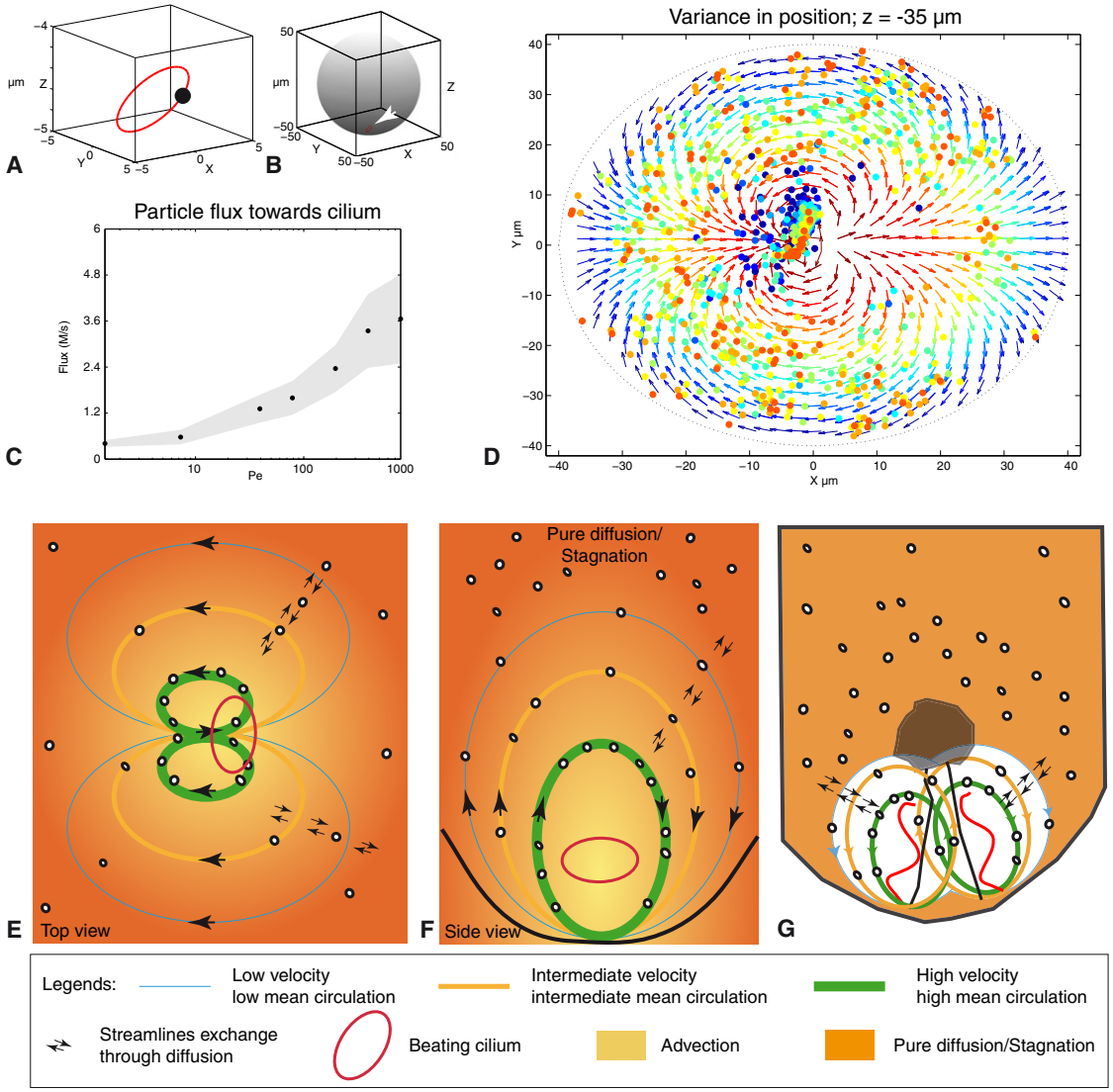


**Figure 4. Inner Ear Viscous Flow Model**

(A and B) The hydrodynamic model of the inner ear represents the cilium by a small sphere (black dot) moving on a tilted elliptical trajectory (in red), placed at the bottom (0.0,−45 μm) of the inner ear (white arrow), which is represented by a larger sphere, with a radius of 50 μm (B).

(C) The flux of particles (Mols/sec) toward the cilium-sphere as a function of *Pe*. Particles are released along the edge of the inner ear-sphere at $t = 0$, and the average time particles take to reach the cilium is computed at different cilium frequencies, which is directly related to the *Pe*. The gray shaded region is the standard deviation of flux.

(D) Maximum projection of the time-averaged flow field (arrows) inside the inner ear-sphere along the planes $z < -35$ μm, for cilia frequency of 54 Hz. This plane illustrates the principle of cilium-induced flow. The coloring of the arrows indicates speed in logarithmic units. Red arrows indicate fast velocities (~60 μm/s), whereas blue arrows indicate slow velocities (~1 μm/s). Dots indicate the average position of a particle in a 100 ms interval. The color of the dot shows the variance of position in that 100 ms interval, in linear units. Near the cilium, which is located in at (0,0), particles are orange indicating a small degree of position variance (<1 $\mu m^2$), whereas particles are blue immediately outside the location of the cilium (>10 $\mu m^2$). Particles closest to the cilium circulate around the cilium many times before diffusing away, due to entrainment, resulting in a small position variance (orange), whereas particles immediately outside the cilium are advected toward the cilium, so their position variance is high (blue). Particles on the edge of (D) are primarily orange and yellow because they are far away from the cilium and therefore do not feel its effect; thus, their variance is determined for the most part by temperature. See Movie S6 for a demonstration of the simulation.

(E) Schematic representation of flow field in (D) and the orthogonal flow field (x-z plane).

(F) In the x-y plane (E), the flow is dipole-like, whereas flow in the x-z plane (F) is circulatory. Particles traveling along each streamline have uniform probability of leaving it, due to Brownian motion. However, faster velocities (green lines) shape particles' trajectories into a stereotyped flow pattern, resulting in entrainment.

(G) Schematic representation of flow field at work in the inner ear (side view) summarizing the knowledge gained from model. The white object in the middle is the otolith; the two red wavy lines represent motile cilium. Black lines supporting the otolith are tether cilia.

away through a dipole-like flow pattern (Figures 4E and 4F). Altogether, the increasing velocity along inner radii increases advective stirring around the otolith. Brownian motion is still, of course, a requirement for enhanced particle circulation: without diffusion, particles do not exchange streamlines and cannot therefore get closer to the otolith ($<N_{circ}>$ goes to 0). Moreover, particles that are on the size scale of velocity gradients in shear flow potentially experience a force directed toward higher velocities (Gavze and Shapiro, 1997). Thus, our model demonstrates that cilia can increase spherule transport through a dipole-like flow and due to the quick decay of flows in viscous fluids a stagnation zone is apparent in the immediate vicinity, thereby suggesting that a mechanical mechanism can account for the observed biased location of otolith formation near motile cilia (Figure 4G).

## DISCUSSION

Through the application of in vivo visualization technologies, we have taken a closer look at the flow generated by beating cilia in the zebrafish inner ear and identified two hydrodynamic features explaining the effects of flow during otolith formation: (1) transport toward tether cilia and subsequent rapid reduction in flow propagation results in a transition to Brownian motion, which leads to preferential spherule localization near the tether cilia and (2) high velocities nearer to the base of the otolith results in asymmetric shape production of the growing otolith. These features clarify the role of advection in the inner ear cavity showed previously (Colantonio et al., 2009) and suggest a better model for otolith assembly whereby the role of diffusion is included, and whereby the shape of the otolith is directly coupled to the flow forces. Here, motile cilia transports precursor particles toward tether cilia accounting for number, position, and size (Colantonio et al., 2009), and locally stirs the fluid (Riley et al., 1997), accounting for the flat bottom shape of the otolith. Since it is clear from zebrafish mutants that otolith shape is highly stereotyped and is critical for sensory organ function in the inner ear (Hughes et al., 2006; Nicolson, 2005; Schibler and Malicki, 2007; Sollner et al., 2003), we speculate that the flat-bottomed shape of the otolith allows orthogonal cilia implantation within the otolith that could maximize sensitivity of stereocilia bundles to linear displacements (Karavitaki and Corey, 2010).

The hydrodynamics mediated by inner ear cilia is similar in action to what has been described in bi-flagellae *Chlamydomonas reinhardtii* and *Chlamydomonas* colony *Volvox carteri*, which uses the same type of linear advection-diffusion system to drive metabolite uptake and waste exchange (Short et al., 2006; Solari et al., 2006). The flux toward the cilia, as well as spherule entrainment, depends on the particular physical boundaries of the inner ear wall, the frequency of the cilia, and the ability of the tether cilia to immobilize spherules. As a consequence, these observations suggest a basic mechanism where the self-organizing properties of otolith formation could solely depend on the hydrodynamics mediated by cilia, diffusion and the self-aggregation properties of the spherules. It is thus tempting to speculate that changes in the inner ear morphology will have a direct effect on hydrodynamics and can account for the variability of otolith shape observed in teleosts.

Ciliated organs affect the distribution of many other biological products in vertebrates' cavities, such as signaling molecules during stem cell migration in the brain (Sawamoto et al., 2006) and in the left right organizer (Okada et al., 2005; Schweickert et al., 2007) where the fluidic motion is also highly stereotyped. However, the complexity of cilia activities as well as the multiplicity of biological outcomes they can control during development is far from being understood (Cartwright et al., 2009). Our study demonstrates that the use of noninvasive optical methods of probing flow are accurate enough to precisely address microscopic flows. Furthermore, as there is increasing evidence that congenital diseases are rooted in multifactorial processes involving cilia in the developing embryo (Gerdes et al., 2009), precise flow probing becomes critical to understand the biological principles that govern cilia driven flow and their potential involvement in diseases. In this context, our method to quantify the dynamics of flow could be applied to study cilia driven flows in a variety of developing organs.

## EXPERIMENTAL PROCEDURES

### Bright-Field Imaging

Imaging was performed on a home built microscope incorporating a 60× 1.2 NA Olympus IR corrected water immersion objective, coupled with a 200 mm focal length tube lens. Either a Basler A602f CMOS camera (10 μm pixel size) or a Prosilica GC1380H camera (6.4 μm pixel size) was used for imaging. Data were taken using custom Matlab scripts. Embryos were mounted in agarose using a micromachined mold so that the neural tube was facing the objective for the flow mapping using PIV (dorsal view, Figures 1G and 1H). Side views of the otolith were obtained by mounting the embryos slightly on the side so that the neural tube was at a 45 degree angle relative to the objective (side view, Figures 1, 2D, 2F, and 2I).

### Particle Image Velocimetry of the Flow Field

By shining focused laser light (1064 nm, 100 mW) through the microscope objective (as described under "bright-field imaging") for a few seconds (<30 s), particles were accumulated to perform particle image velocimetry (PIV). PIV was calculated over 8×8 subsamples of the movies using custom Matlab scripts. The imaging frame rate was 30 Hz. The embryos showed no obvious signs of damage from the laser. Correlation was performed between two adjacent frames in time. The PIV algorithm also detects otolith movement, causing arrows to show up in Figures 1F and 1G; the otolith itself is always moving. The short period of time, and low laser power employed, were not enough to cause irreversible particle aggregation, compared with the powers and times used in Riley et al. (1997).

### Blinking Optical Trapping

A 1064 nm laser was used in conjunction with an acousto-optic deflector (AOD) utilizing digitally synthesized frequencies. A custom Labview program was used to control the modulator. We found that the best switching frequency for single spherule trapping and tracking was 10 Hz. The laser output power (after the AODs) was 100 mW. A 532 nm notch filter was used to block laser light. Imaging was performed as described above under "bright-field imaging," at 492 fps. Microscope construction was the same as used in PIV (above).

### Laser Inactivation of Cilia Beat

A 532 nm laser at 1 W focused on beating cilia was used in 30 s increments to evaluate if the cilia had been inactivated. Typically, cilia were illuminated for 1 min to reach motion stasis. Otolith shapes were checked 1, 2, or 5 hr, and 17 hr after ablation.

### Otolith Segmentation

We regularized the otolith orientation by rotating the otolith along an axis defined by the tether cilia. The midpoint of the otolith was then determined

by the largest width along an axis perpendicular to the tether cilia. We next fitted a circle to the otolith using the largest width as a constraint and calculated the sum of squared residuals (SSR). Since the expected distribution of SSR is unlikely to be Gaussian, we employed a bootstrap algorithm to determine the significance of the difference of the SSR means between control and laser treated embryos (see Supplemental Experimental Procedures for more details).

### Analysis of BOTs

Using Matlab, one-dimensional Brownian dynamics simulations of a particle released by a trapping laser and subjected to a sinusoidal external force were performed. The resulting mean squared displacement was compared with the analytical result and demonstrates near exact agreement (see Supplemental Experimental Procedures). Since the tracked cilia tips also moved according to an approximate sinusoidal motion, we fitted the BOTs movies to the same analytical result and extracted the parameters. For BOTs analysis, depth of focus does not affect data analysis, as long as we could find the centroid of the particle, since we only measured lateral displacements. If the centroid could not be found, then the data was discarded. Depth of focus of images was 1 micron.

### Simulations of Flow and Diffusion

We used Matlab to compute the velocity field inside a sphere according to the Green's function solution to Stokes' equation. We used a spherical cilium similar to that of Vilfan et al. (see Supplemental Experimental Procedures). The velocity field was then incorporated into a finite-difference Langevin equation as an external force that impinges upon the Brownian particles of 1 μm in diameter. The simulation was run until it reached a statistically stationary state. *Pe* was defined based upon the largest velocity in the simulation; i.e., the tip of the cilium.

## SUPPLEMENTAL INFORMATION

Supplemental Information includes Supplemental Experimental Procedures, one figure, and seven movies and can be found with this article online at doi:10.1016/j.devcel.2010.12.006.

## ACKNOWLEDGMENTS

We are grateful to the Fraser and the Phillips laboratory for stimulating discussions and help throughout the course of the project. We thank K. Hill, D. Riveline, and A. Vilfan for thoughtful comments on the manuscript. We are grateful to R. Phillips, H. J. Lee, L. Trinh, K. Hill, and M. Liebling for sharing reagents. We also want to thank the IGBMC, Institut de Génétique et de Biologie Moléculaire et Cellulaire for assistance. J.V. is supported by the Human Frontier Science Program (HFSP), D.W. was supported by the NIH Medical Scientist Training Program at UCLA/Caltech.

Received: August 10, 2010
Revised: October 13, 2010
Accepted: November 27, 2010
Published: February 14, 2011

## REFERENCES

Blasiole, B., Canfield, V.A., Vollrath, M.A., Huss, D., Mohideen, M.A., Dickman, J.D., Cheng, K.C., Fekete, D.M., and Levenson, R. (2006). Separate Na,K-ATPase genes are required for otolith formation and semicircular canal development in zebrafish. Dev. Biol. *294*, 148–160.

Bouligand, Y. (2004). The renewal of ideas about biomineralisations. Comptes. Rendus. Palevol. *3*, 617–628.

Cartwright, J.H., Piro, O., and Tuval, I. (2009). Fluid dynamics in developmental biology: moving fluids that shape ontogeny. HFSP J. *3*, 77–93.

Clendenon, S.G., Shah, B., Miller, C.A., Schmeisser, G., Walter, A., Gattone, V.H., 2nd, Barald, K.F., Liu, Q., and Marrs, J.A. (2009). Cadherin-11 controls otolith assembly: evidence for extracellular cadherin activity. Dev. Dyn. *238*, 1909–1922.

Colantonio, J.R., Vermot, J., Wu, D., Langenbacher, A.D., Fraser, S., Chen, J.N., and Hill, K.L. (2009). The dynein regulatory complex is required for ciliary motility and otolith biogenesis in the inner ear. Nature *457*, 205–209.

Gavze, E., and Shapiro, M. (1997). Particles in a shear flow near a solid wall: effect of non- sphericity on forces and velocities. Int. J. Multiph. Flow *23*, 155.

Gerdes, J.M., Davis, E.E., and Katsanis, N. (2009). The vertebrate primary cilium in development, homeostasis, and disease. Cell *137*, 32–45.

Hughes, I., Thalmann, I., Thalmann, R., and Ornitz, D.M. (2006). Mixing model systems: using zebrafish and mouse inner ear mutants and other organ systems to unravel the mystery of otoconial development. Brain Res. *1091*, 58–74.

Karavitaki, K.D., and Corey, D.P. (2010). Sliding adhesion confers coherent motion to hair cell stereocilia and parallel gating to transduction channels. J. Neurosci. *30*, 9051–9063.

Lin, B., Yu, J., and Rice, S.A. (2000). Direct measurements of constrained brownian motion of an isolated sphere between two walls. Phys. Rev. E Stat. Phys. Plasmas Fluids Relat. Interdiscip. Topics *62*, 3909–3919.

Maul, C., and Kim, S. (1994). Image systems for a Stokeslet inside a rigid spherical container. Phys. Fluids *6*, 2221.

Nicolson, T. (2005). The genetics of hearing and balance in zebrafish. Annu. Rev. Genet. *39*, 9–22.

Okada, Y., Takeda, S., Tanaka, Y., Belmonte, J.C., and Hirokawa, N. (2005). Mechanism of nodal flow: a conserved symmetry breaking event in left-right axis determination. Cell *121*, 633–644.

Pisam, M., Jammet, C., and Laurent, D. (2002). First steps of otolith formation of the zebrafish: role of glycogen? Cell Tissue Res. *310*, 163–168.

Riley, B.B., Zhu, C., Janetopoulos, C., and Aufderheide, K.J. (1997). A critical period of ear development controlled by distinct populations of ciliated cells in the zebrafish. Dev. Biol. *191*, 191–201.

Sawamoto, K., Wichterle, H., Gonzalez-Perez, O., Cholfin, J.A., Yamada, M., Spassky, N., Murcia, N.S., Garcia-Verdugo, J.M., Marin, O., Rubenstein, J.L., et al. (2006). New neurons follow the flow of cerebrospinal fluid in the adult brain. Science *311*, 629–632.

Schibler, A., and Malicki, J. (2007). A screen for genetic defects of the zebrafish ear. Mech. Dev. *124*, 592–604.

Schweickert, A., Weber, T., Beyer, T., Vick, P., Bogusch, S., Feistel, K., and Blum, M. (2007). Cilia-driven leftward flow determines laterality in Xenopus. Curr. Biol. *17*, 60–66.

Short, M.B., Solari, C.A., Ganguly, S., Powers, T.R., Kessler, J.O., and Goldstein, R.E. (2006). Flows driven by flagella of multicellular organisms enhance long-range molecular transport. Proc. Natl. Acad. Sci. USA *103*, 8315–8319.

Solari, C.A., Ganguly, S., Kessler, J.O., Michod, R.E., and Goldstein, R.E. (2006). Multicellularity and the functional interdependence of motility and molecular transport. Proc. Natl. Acad. Sci. USA *103*, 1353–1358.

Sollner, C., Burghammer, M., Busch-Nentwich, E., Berger, J., Schwarz, H., Riekel, C., and Nicolson, T. (2003). Control of crystal size and lattice formation by starmaker in otolith biomineralization. Science *302*, 282–286.

Svoboda, K., and Block, S.M. (1994). Biological applications of optical forces. Annu. Rev. Biophys. Biomol. Struct. *23*, 247–285.

Vilfan, A., and Julicher, F. (2006). Hydrodynamic flow patterns and synchronization of beating cilia. Phys. Rev. Lett. *96*, 058102.

Wilt, F.H. (2005). Developmental biology meets materials science: morphogenesis of biomineralized structures. Dev. Biol. *280*, 15–25.